Journal of Intelligent & Robotic Systems (2022) 105: 23
https://doi.org/10.1007/s10846-022-01638-9

SHORT PAPER

Design and Analysis of a Novel Swimming Mechanism Inspired from Frogs

Yucheng Tang [1] · Xiaolong Yang [1] · Wei Liu [2] · Lizhi Qi [1] · Yan Wang [3] · Yulin Wang [1]

Received: 9 February 2021 / Accepted: 12 April 2022 / Published online: 13 May 2022

Abstract
This article presents a design of a novel swimming mechanism based on a linkage mechanism. The generated motions of the proposed mechanism mimic the purely aquatic locomotion of frogs such as *Xenopus laevis (X. laevis)*, including both the motions of the hind legs and the webbed foot. A six-bar linkage mechanism is employed in this study combing with a spatial linkage mechanism to simplify the overall mechanism. Attributes to the optimal design, the number of Degrees of Actuations (DoA) reduces to two in each hindlimb, which realizes miniaturization in the current study. Kinematic analysis is conducted to analyze the locomotion of the spatial mechanism. The hydrodynamic model based on the blade element theory is established to estimate the swimming performance of the designed mechanism. The peak thrust (approximately 0.2 *N*) is dramatically larger than the minimum drag (−0.023 *N*) observed in the experiment which increases the efficiency of the prototype's swimming.

Keywords Frog-inspired swimming mechanism · Hybrid linkage mechanism · Kinematic analysis · Hydrodynamic model

1 Introduction

Implementing biomimetics or bioinspired features into robotic systems has become a new solution to solve the problems of kinematics, dynamics, and control [1, 2]. No matter what is employed, bioinspired mechanical structure or mimicking the locomotion of natural creatures, they make the specially designed robots acquire the ability to complete difficult tasks. The vertical wall climbing based on gecko-inspired toes is presented in [3] while high efficient underwater swimming is achieved by combining a compliant tail design with proper undulatory locomotion in [4]. Flying ability is acquired by morphologically mimicking the wing structures of bats [4–6], amphibious locomotion by utilizing specially designed structures inspired by basilisk lizards [7–9], salamanders [10, 11], et al.

Frogs are one of the most wonderful animals which mostly use their hindlimbs to acquire the capabilities of jumping and swimming. The reactive force propelled the body of the frog in both terrestrial and aquatic environments when the hindlimb contacts the ground and the water [12]. The strategy of frogs' locomotion by mainly using their hindlimbs helps the design of bio-inspired robots to reduce the number of actuators. The swimming locomotion of frogs is dominantly on account of their hindlimbs as their forelimbs are used for support and steering [13]. The swimming locomotion with dual-limb cooperation is more stable and more maneuverable compared to the locomotion of fish's tail oscillation which produces the lateral force during swimming. The swimming gaits of frogs are divided into synchronous swimming and asynchronous swimming attributed to the cooperation of the powerful hindlimbs. With synchronous swimming, frogs can have a faster speed to escape from their predators when the asynchronous swimming gait works more efficiently [14]. Apart from the hind legs, the webbed foot plays a significant role in frogs' swimming as well. The fully expanded area of the webbed foot helps the hindlimb produce maximized thrust when the legs extend. The drag produced on the foot is minimized as the frogs shrink their foot with the flexion of the hindlimbs.

✉ Yulin Wang
wyl_sjtu@126.com

[1] School of Mechanical Engineering, Nanjing University of Science and Technology, Nanjing 210094, China

[2] State Key Laboratory of Intelligent Manufacturing System Technology, Beijing Institute of Electronic System Engineering, Beijing 100854, China

[3] Department of Computing, Mathematics and Engineering, University of Brighton, Brighton BN2 4GJ, UK

These interesting characteristics of the frog's swimming attract more researchers to design bioinspired swimming robots and analyze the propulsion mechanism. Jyotsna et al. [13] proposed a cam follower mechanism with a tendon-pulley mechanism to mimic the joint behaviors of the limbs. Multiple types of locomotion such as terrestrial and aquatic locomotion are assumed to be obtained from the additional degree of freedom (DoF) for the transformation of the hindlimbs. The complex mechanism troubles the manufacturing of robots. Fan et al. [15] designed a swimming robot inspired by frogs. Each leg of the robot is composed of two groups of pneumatic muscles with an antagonistic configuration. By controlling the three-DoF leg, the robot can mimic the swimming gaits of swimming frogs. The webbed foot is designed by assembling a water-proof motor at the end of the foot. The control is complex as many pneumatic actuators are integrated. The size of the robot is limited by the pneumatic muscles. An improved swimming robot based on pneumatic technology is reported in [16]. The most significant improvement is the articulated pneumatic soft actuators, which minimize the size of the frog-inspired swimming robot. Although the size is decreased with the customized soft actuator, the joints of the hindlimb are still actuated separately. The massive actuators make the robot structure bulky and it causes difficulties in controlling the robot. Based on the study of Richards [17], the thrust of the aquatic frogs is mostly induced by feet rotation compared to their translational motion, we previously designed a swimming robot based on dielectric elastomer with only one rotation degree of freedom in each limb [18]. Although the dielectric elastomer actuator can help the leg structure achieve large angular deformation, the output force is normally small due to the properties of the dielectric elastomer minimum energy structure [19–21]. Consequently, the thrust is not sufficient to drive the robot when the robot is fully submerged in water. Hereby, we concentrate on the structure design of the hindlimb of the swimming robot instead of the actuator which is capable to help the robot achieve sufficient thrust. Motors are used as the candidates to drive the designed leg structure for robustness and simple employment in the robot system.

The frogs benefit from the complex biological structures composed of multiple ball-and-socket-like joints of abundant degrees of freedom (DOFs) such as flexion/extension, abduction/adduction, and exterior/interior rotation which results in a flexible workspace [22–24]. To employ the biological characteristics in robots, further reduction of the actuating component is needed. Biological kinematic synergies are selected as the proper solution to design the robot inspired by creatures from abundant DOFs. Applying principal component analysis (PCA), *Bat-Bot* (B2) [6] is designed employing the combination of a spatial flapping mechanism and a folding and unfolding mechanism based on a planar four-bar crank-rocker. Another representative case where biological synergy is employed is the jumping robot Salto, where an optimized planar eight-bar linkage of merely revolute joints is designed to mimic the hindlimb of *Galago senegalensis* [25]. These outstanding cases reveal that the design of bio-inspired robots with synergy technology can minimize the number of DoAs.

This study aims to design a novel mechanism learning from the amphibious frogs with a focus on their hindlimbs to reduce the complexity of the swimming robot design. The locomotion analysis of frogs o aquatic environments is conducted to discover the swimming mechanism in the frontal and the transverse plane. Synthesis design is employed to reduce the number of actuators to provide rotational actuation. A novel optimal design method is employed for the six-bar linkage synergistic design to mimic the locomotion of frogs' feet. The spatial mechanism is employed in the hybrid mechanism design to acquire the spatial motion of the footpad where a minimum quantity of input is needed. To validate the adaptability of the design in aquatic environments, a hydrodynamic analysis based on the blade element theory is built to estimate the thrust generated in the power swimming phase.

This paper is structured as follows: locomotion analysis of aquatic frogs using a footpad is discussed in Section 2. The biological mechanism design including the planar mechanism optimization and the hybrid mechanism design is mentioned in Section 3. Section 4 presents the kinematic and the hydrodynamic analysis of the designed mechanism. The experimental validation is included in Section 4 as well. The conclusion is in the final section.

2 Locomotion Analysis of Aquatic Frogs

Figure 1 shows the schematic of the skeletal mechanism of an amphibious frog using the half body of a frog isolated by the sagittal plane. The posture of a swimming frog's footpad that is parallel to the transverse plane is changed at the beginning of each stroke as presented in Fig. 1(A). Although the foot motion is composed of translational and rotational components, the motion of each joint of the hindlimb can be treated as 2D pivot joints as reported by Richards [17, 26, 27] in which the translational motion contributes much less than the rotational motion. Separated actuation in each group of hindlimbs is needed as the swimming locomotion reveals that both synchronous and asynchronous locomotion exist, generating perspective swimming performance [26]. As paddle swimmers, frogs use the deformable projected area on the webbed feet to improve their swimming efficiency. Both synchronous and asynchronous locomotion can be divided into three cyclic phases. At the beginning of the propulsion phase, the hindlimb "folded" and the webbed feet fully expanded for maximizing the thrust force when the hindlimb extends. Attributing to a streamlined body, the legs are fully extended, and the webbed feet are fixed in the direction parallel to the

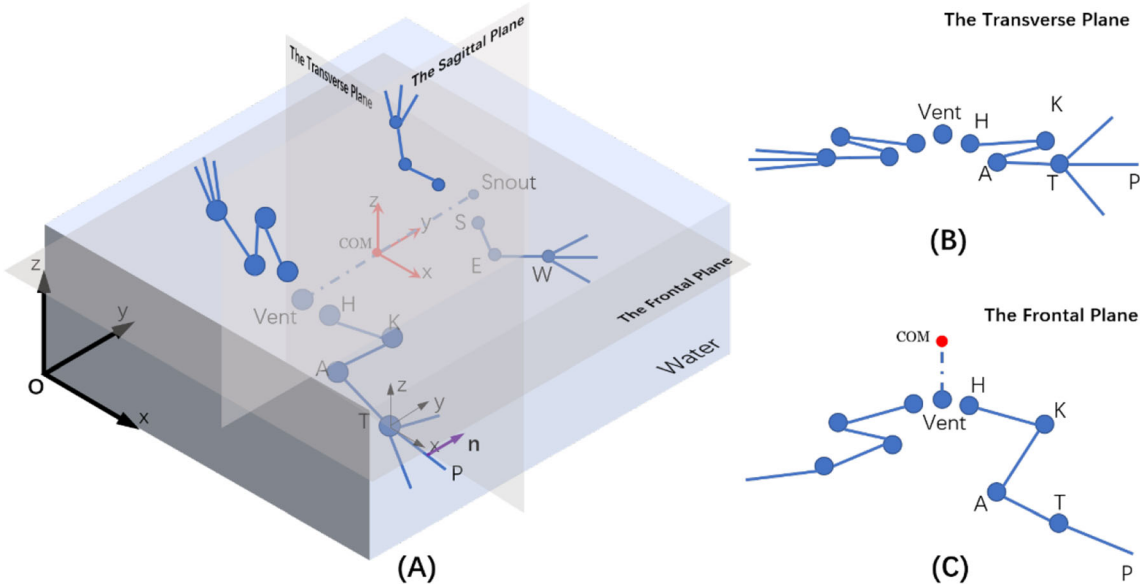

Fig. 1 Skeletal schematic of an amphibious frog in aquatic mode. In (**A**), the normal vector **n** is parallel to the moving direction along the **y** axis in water. (**B**) shows the view of the hindlimb skeleton system in the Transverse Plane while the view of the Frontal plane is shown in (**C**)

moving direction in the glide phase. To be ready for the next propulsion phase, the hindlimb flexes to the initial position with the contracted webbed feet to minimize the drag produced on the feet during the recovery phase [18]. By decomposing the foot motion of different species of frogs into translational and rotational motion, Richards reported that the thrust of aquatic species, for example, *X. laevis*, is mostly induced by foot rotation whereas foot translation contributes much less significantly [17]. His later study proved this hypothesis that the propulsive strategy of *X. laevis* is mostly rotation-powered swimming [26]. Based on his theory, the multiple joints-based extension for propulsion can be simplified as a single rotation in each leg of aquatic frogs. The morphing of the projected area in webbed feet can generate propulsive swimming motion by making the thrust generated in the propulsion phase larger than the drag encountered in the recovery phase.

From the analysis above, two principal motions are extracted in the transverse and the frontal plane. In the frontal plane, a mechanism is needed to generate the planar motion such as extension and flexion of the hindlimb, led by the rotation in the hip joint, knee joint, ankle joint, and tarsometatarsal joint. Apart from the planar mechanism in the frontal plane, the webbed foot of the robot is needed to morph the projected area using another DoA. To mimic the strategy of the aquatic frogs used in swimming, in the power swimming phase, the area of the webbed foot needs to keep maximized whereas, in the recovery phase, it keeps minimized to reduce the drag on their feet. Hence, the whole mechanism design can be split into the planar motion part and the part for the posture switch of the footpad. Figure 2 presents the prototype of the designed swimming mechanism, the hindlimbs are made up of a planar six-bar linkage to mimic the hindlimb locomotion of an aquatic frog. The six-bar linkage is merely composed of revolute joints which are easy to configure and the motion of the linkage is actuated by one joint by Actuator 1. All links are 3D printed and they are made of polylactic acid (PLA). The purely aquatic frog *X. laevis* is selected and the linkage parameters are optimized to track the trajectory of *X. laevis's* foot. The webbed foot mechanism is slightly different from the real frogs by connecting the six-bar linkage with a spatial linkage mechanism actuated by Actuator 2 which is a fixed-axis rotation. The design procedure is detailed in Section 3.

3 Mechanical Design

3.1 Hindlimb Design Based on Six-Bar Linkage

According to the analysis in Section 2, the motion of the frog's foot is generated by the cooperation of the hip, knee, and ankle joints of the hindlimbs. In the conventional design of bio-inspired robots, each joint is connected serially and actuated each joint individually to mimic the locomotion of the real animal. Despite the intuitionistic and simple design procedure, the control of the numerous actuators is typically complex and when the redundant workspace is wasted.

Planar linkage mechanisms including Four-bar, six-bar, and eight-bar linkage constrained with Revolute-Revolute (RR) chain have been widely researched [28–31], for which the focus is on the output of a specific point or link with one DoF actuation instead of the actuation of each joint. Inspired from these successful designs, we employ a six-bar linkage mechanism to explore the design to mimic the leg motion of

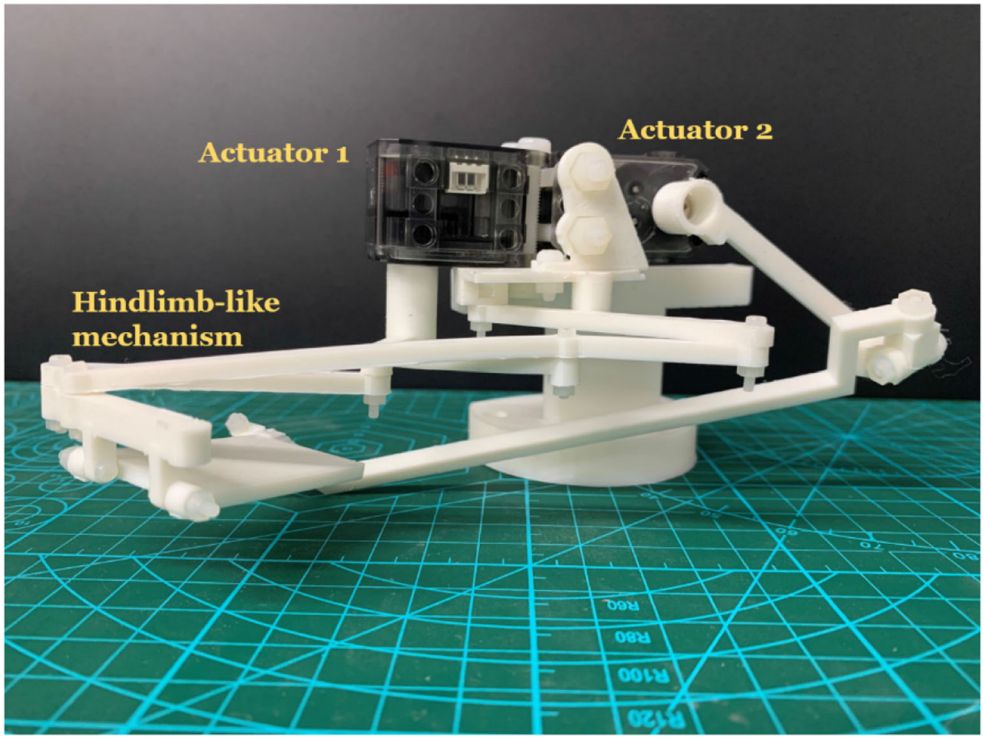

Fig. 2 The prototype of the spatial mechanism to mimic the hindlimbs of aquatic frogs

swimming frogs. Four-bar linkage is not utilized as the design candidate due to its limited number of design parameters while eight-bar linkage is not considered it needs massive computational cost in its design. A six-bar linkage mechanism is proposed from the skeletal structure of a frog's hindlimb, which consists of the femur, tibiofibula, tarsus, and phalanx. As shown in Fig. 3(A), the femur of *X. laevis* is connected to the body with the hip joint while the knee joint connects the tibiofibula and femur. The ankle joint connects the tarsus and the tibiofibula while the tarsometatarsal joint connects the phalanx and tarsus [32]. The output motion of the foot is generated by the corporative actuations in these four joints as demonstrated in Fig. 3(B). Two ternary links such as link $J_1J_4J_6$ and link $J_3J_6J_7$ are added to close the topology loop of the linkage mechanism. The tarsus and phalanx are considered as a rigid body without relative movement to reduce the

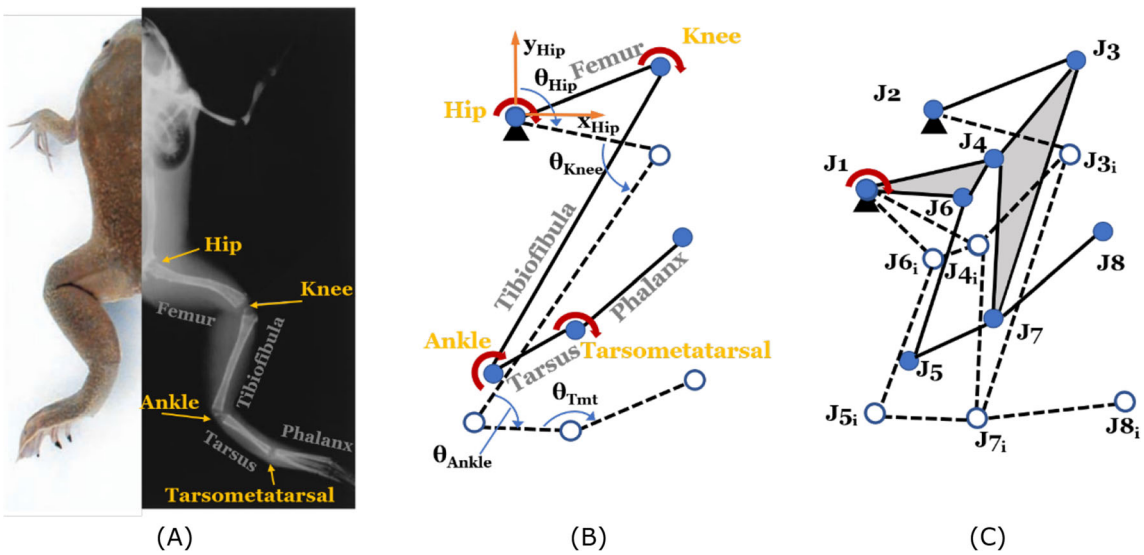

Fig. 3 Six-bar linkage design schematic from the skeleton of hindlimbs. (**A**). The hindlimb physiology of *X. laevis*. (**B**). Serial configuration of the RR linkage design (**C**). Six-bar linkage design with one-DOA

complexity of the whole structure. The link J_7J_8 works as the foot where the joint J_7 mimics the tarsometatarsal and joint J_8 mimics the end of the longest phalange. Thus, a six-bar linkage of one DoA is formed as revealed in Fig. 3(C). As demonstrated in Fig. 3, the circular shapes filled with blue denote the joints in the initial position while the hollow-circular shapes show the relevant positions when actuation input is revealed as the red arc. The dash lines represent the current position of the links while the solid ones are in the initial position. It is possible to trace the approximately same output trajectories of the foot composed of phalanx in the two different configurations despite the different number of DoAs.

3.1.1 Forward Kinematic Analysis of the Planar Six-Bar Linkage

The forward kinematic analysis is conducted to acquire the relationship between the input (one DoF rotation) and the output of the foot. The coordinate system of the center of mass (CoM) $\{O_{\mathrm{CoM}}\}$ is built as shown in Fig. 4(A) where $\mathbf{O_{CoM}}$ $\mathbf{X_{CoM}}$ is parallel to the symmetrical axis of the body. $\{O_{J_1}\}$ is translated from $\{O_{\mathrm{CoM}}\}$ without rotation. It is obvious that the formed six-bar linkage is composed of a four-bar linkage loop J_1- J_2- J_3- J_4 and two bar linkage J_5- J_6 and J_5- J_7. In the four-bar loop, the position of J_{4i} in $\{O_{J_1}\}$ with the input rotation about the z-axis in J_1 can be written as

$$[J_{4i}]_{O_{J_1}} = Rot_z(u_i)[J_4]_{O_{J_1}} \tag{1}$$

In Eq. (1), Rot_z is the rotation matrix about the **z**-axis and $Rot_z(\theta) = \begin{bmatrix} cos(\theta) & -sin(\theta) \\ sin(\theta) & cos(\theta) \end{bmatrix}$. The arrow of the rotation in the figures of this work starts at the reference position and ends at the current position and the counterclockwise direction is the positive direction.

The Cartesian coordinates of $[J_{3i}]_{O_{J_1}}$ is

$$[J_{3i}]_{O_{J_1}} = Rot_z(w_i)\left([J_3]_{O_{J_1}} - [J_2]_{O_{J_1}}\right) + [J_2]_{O_{J_1}} \tag{2}$$

The length of the link J_3J_4 keeps constant as

$$\left\|[J_{3i}]_{O_{J_1}} - [J_{4i}]_{O_{J_1}}\right\| = \left\|[J_3]_{O_{J_1}} - [J_4]_{O_{J_1}}\right\| = l_{J_3J_4} \tag{3}$$

Instead of directly solving the equations constituted by (1), (2), and (3), J_{3i}can be derived from the geometry point of view according to the four-bar loop extracted in Fig. 4(B). The point J_{3i} is the intersection of two circles shown circled in red. Another intersection point J_{3i}' is neglected as with the solution, the configuration of the four-bar loop is not practical. These two solutions are symmetrical about J_2J_{4i}. Hence, $[J_{3i}]_{O_{J_1}}$ can be calculated as

$$[J_{3i}]_{O_{J_1}} = \frac{l_{J_2J_3}}{l_{J_2J_{4i}}} Rot_z(\mathrm{m}_i)\left([J_{4i}]_{O_{J_1}} - [J_2]_{O_{J_1}}\right) + [J_2]_{O_{J_1}} \tag{4}$$

In Eq. (4), $m_i = arccos\frac{l_{J_2J_{4i}}{}^2 + l_{J_2J_3}{}^2 - l_{J_3J_4}{}^2}{2J_2J_{4i}l_{J_2J_3}}$ as l_{23} and l_{34} keep constant with the input rotation.

According to (4), $[J_{7i}]_{O_{J_1}}$ is written as below,

$$[J_{7i}]_{O_{J_1}} = \frac{l_{J_3J_4}}{l_{J_3J_7}} Rot_z(e)\left([J_{4i}]_{O_{J_1}} - [J_{3i}]_{O_{J_1}}\right) + [J_{3i}]_{O_{J_1}} \tag{5}$$

The strategy for finding J_{5i} and avoiding the multiplicity is close to which used in finding J_{3i}. Consequently, $[J_{5i}]_{O_{J_1}}$ is

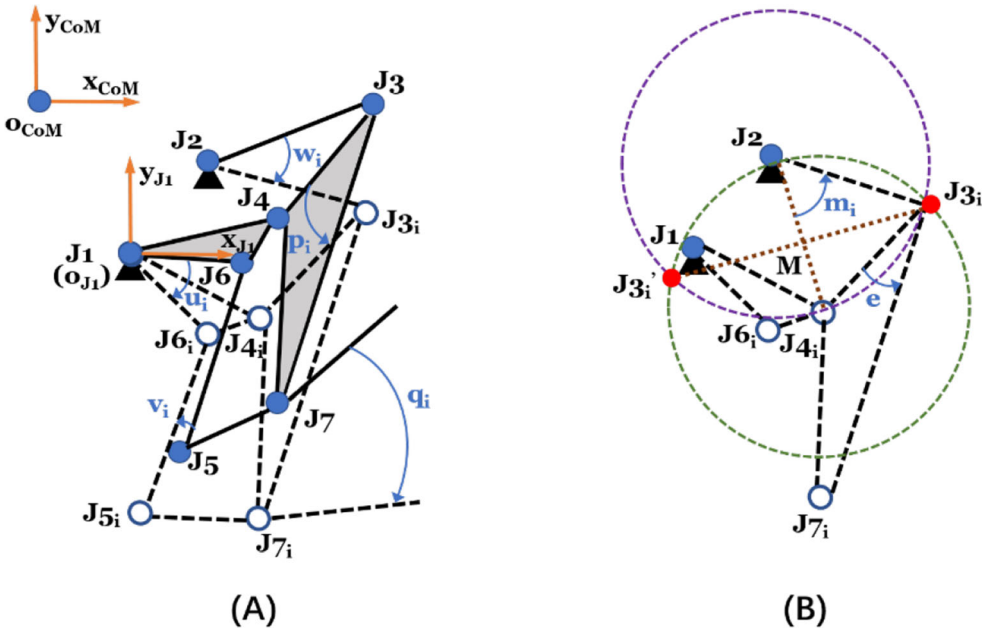

Fig. 4 Kinematic schematic of the six-bar linkage. (**A**). Movement of the six-bar linkage (**B**) Solutions of J_{3i} in four-bar loop J_1- J_2- J_3- J_4

calculated as

$$[J_{5i}]_{O_{J_1}} = \frac{l_{J_5J_6}}{l_{J_{6i}J_{7i}}} Rot_z(-n_i)\left([J_{7i}]_{O_{J_1}} - [J_{6i}]_{O_{J_1}}\right) + [J_{6i}]_{O_{J_1}} \quad (6)$$

In Eq. (6), $n_i = arccos\frac{l_{J_{6i}J_{7i}}{}^2 + l_{J_5J_6}{}^2 - l_{J_5J_7}{}^2}{2l_{J_{6i}J_{7i}}l_{J_5J_6}}$ and $[J_{6i}]_{O_{J_1}} = Rot_z(u_i)[J_6]_{O_{J_1}}$.

The rotation of J_7J_8 can be calculated from Eq. (7).

$$q_i = k \cdot arccos\frac{\left([J_{7i}]_{O_{J_1}} - [J_{5i}]_{O_{J_1}}\right) \cdot \left([J_7]_{O_{J_1}} - [J_5]_{O_{J_1}}\right)}{l_{J_5J_7}{}^2} \quad (7)$$

Where $k = \frac{\left(\left([J_7]_{O_{J_1}} - [J_5]_{O_{J_1}}\right) \times \left([J_{7i}]_{O_{J_1}} - [J_{5i}]_{O_{J_1}}\right)\right)_z}{\left|\left(\left([J_7]_{O_{J_1}} - [J_5]_{O_{J_1}}\right) \times \left([J_{7i}]_{O_{J_1}} - [J_{5i}]_{O_{J_1}}\right)\right)_z\right|}$ denotes the direction of the rotation when −1 and 1 represent clockwise and counterclockwise, respectively.

3.1.2 Optimization of the Six-Bar Linkage Parameters

The hindlimb morphology of *X. laevis* has been acquired from [26] as well as the joint kinematics. The length of each bone in the hindlimb is presented in Table 1. The joint kinematics of *X. laevis's* hindlimb is demonstrated in Fig. 5. The foot position in $\{O_{Hip}\}$ is predominated by the position of Tmt and θ_{Tmt}. The coordinates of Tmt in $\{O_{Hip}\}$ are given by

$$\begin{cases} [Knee]_{O_{Hip}} = L_{Femur} Rot_z(-\theta_{Hip}) \begin{bmatrix} 0 \\ 1 \end{bmatrix} \\ [Ankle]_{O_{Hip}} = \frac{L_{Tibiofibula}}{L_{Femur}} Rot_z(\theta_{Knee})\left(-[Knee]_{O_{Hip}}\right) + [Knee]_{O_{Hip}} \\ [Tmt]_{O_{Hip}} = \frac{L_{Tarsus}}{L_{Tibiofibula}} Rot_z(-\theta_{Ankle})\left([Knee]_{O_{Hip}} - [Ankle]_{O_{Hip}}\right) + [Ankle]_{O_{Hip}} \end{cases} \quad (8)$$

Thus, the trajectory of the foot in $\{O_{Hip}\}$ can be calculated with Eq. (7) and θ_{Tmt}. The foot motion is planar as the foot is considered as a rigid part and therefore the relationship between θ_{Tmt} and the coordinates of Tmt in $\{O_{Hip}\}$ drawn in Fig. 6 can represent the position of the foot. The parameters of the six-bar linkage including the length and the shape of the links need to be optimized to trace the trajectory of the *X. laevis's* foot. As Fig. 4 indicates, the input rotation is u_i in joint J_1 and the relevant output rotation is q_i, J_7 is set as the Tmt joint. The optimal design should make the relationship

Table 1 Hindlimb morphology of *X. laevis*

L_{Femur} (*mm*)	$L_{Tibiofibula}$ (*mm*)	L_{Tarsus} (*mm*)	L_{Foot} (*mm*)
26	22	11	29

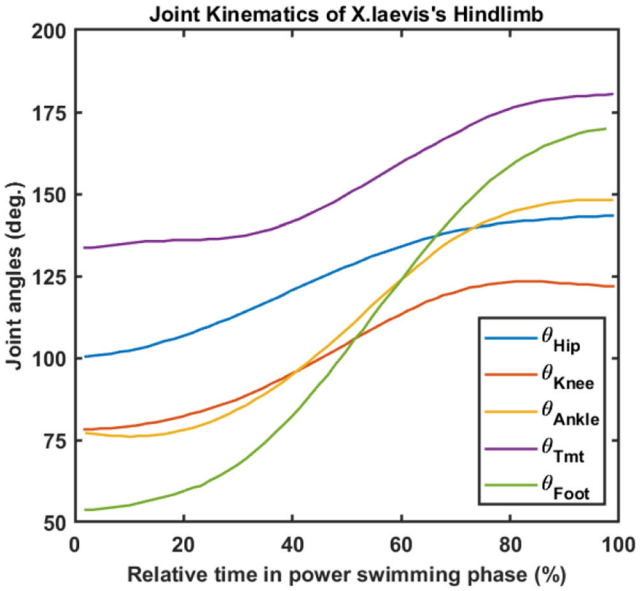

Fig. 5 Joint kinematics of *X. laevis*'s hindlimb

between q_i and $[J_{7i}]_{O_{J_1}}$ approach the relationship shown in Fig. 6 as close as possible when J_1J_2 is the ground link.

As shown in the revised Fig. 3(C), the link formed by J_7 and J_8 works as the foot in the six-bar linkage. The optimization is designed to approach the output trajectories of q_i and J_7 to the foot of the trajectory of the foot of *X. laevis* as shown in Fig. 6. The loop equations are derived as

$$\begin{cases} l_1 : u_i(J_6 - J_1) + v_i(J_5 - J_6) + q_i(J_7 - J_5) = J_{7i} - J_1 \\ l_2 : u_i(J_4 - J_1) + p_i(J_7 - J_4) = J_{7i} - J_1 \\ l_3 : w_i(J_3 - J_2) + p_i(J_7 - J_3) = J_{7i} - J_1 \end{cases} \quad (9)$$

where l_1 represents the loop J_1-J_6-J_5-J_7-J_1 while l_2 and l_3 represents the J_1-J_4-J_7-J_1 and J_2-J_3-J_7-J_2, respectively. Thus, the polynomial system of the six-bar linkage is

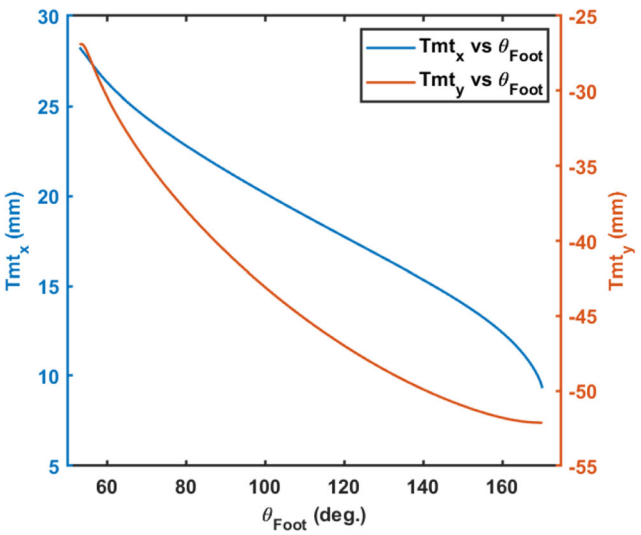

Fig. 6 The relationship between θ_{Tmt} and the coordinates of Tmt in $\{O_{Hip}\}$

$$\begin{cases} u_i(J_6-J_1)+v_i(J_5-J_6)+q_i(J_7-J_5)=J_{7i}-J_1 \\ \overline{u_i(J_6-J_1)}+\overline{v_i(J_5-J_6)}+\overline{q_i(J_7-J_5)}=\overline{J_{7i}-J_1} \\ u_i(J_4-J_1)+p_i(J_7-J_4)=J_{7i}-J_1 \\ \overline{u_i(J_4-J_1)}+\overline{p_i(J_7-J_4)}=\overline{J_{7i}-J_1} \\ w_i(J_3-J_2)+p_i(J_7-J_3)=J_{7i}-J_1 \\ \overline{w_i(J_3-J_2)}+\overline{p_i(J_7-J_3)}=\overline{J_{7i}-J_1} \\ u_i\overline{u_i}=1 \\ v_i\overline{v_i}=1 \\ p_i\overline{p_i}=1 \\ w_i\overline{w_i}=1 \\ i=1,2,\ldots,N \end{cases} \tag{10}$$

where q_i and J_{7i},($i = 1, 2, \ldots, N$) and the desired points which are acquired from the trajectory of the foot of *X. laevis*.

The design parameters are $J_1 - J_6$, u_i, v_i, p_i, w_i and their conjugates. Thus, the number of equations in the polynomial systems is $10N$ while the number of variables is $(6 + 4N) * 2$. To make the polynomial systems square so that a finite set of isolated solution points can be solved computationally, $10N = (6 + 4N) * 2$. Hence $N = 6$ which indicates that six pairs of q_i and J_{7i} can be tracked to make the polynomial system square. Although u_i, v_i, p_i, w_i and their conjugates can be eliminated, the direct computation costs a lot as the total degree of the polynomial system is 2^{60}.

We propose a novel method to design the six-bar linkage mechanism which minimized the difference between the desired trajectories and the output trajectories of q_i and J_{7i}. To keep the units consistent, the objective parameters are converted from q_i and J_{7i} to J_{7i} and J_{8i} where J_{8i} is derived as

$$J_{8i} = q_i(J_8-J_7)+J_{7i} \tag{11}$$

In this method, the six pairs of points in the desired trajectories of *X. laevis*'s foot are selected and they are tracked by J_{7i} and J_{8i} when the length of the link $J_{4i}J_{7i}$ and link $J_{2i}J_{3i}$ and changeable which are drawn in yellow in Fig. 7(B). The objective function of the six-bar linkage is written as

$$\boldsymbol{obj}: minimize\left(\sum_{i=1}^{6}\left(l_{J_4J_7}(x)-l_{J_{4i}J_{7i}}\left(x,J_{7i_{obj}},J_{8i_{obj}}\right)\right)^2+\left(l_{J_2J_3}(x)-l_{J_{2i}J_{3i}}\left(x,J_{7i_{obj}},J_{8i_{obj}}\right)\right)^2\right) \tag{12}$$

where x is the design parameters and $x = [J_{1x}, J_{1y}, J_{2x}, J_{2y}, J_{3x}, J_{3y}, J_{4x}, J_{4y}, J_{5x}, J_{5y}, J_{6x}, J_{6y}]$, $x \in R^{12}$ and J_{7i_obj} and J_{8i_obj} are selected from the desired trajectories and shown in Table 2.

The position of $J_{2i} - J_{6i}$ are derived reversely as J_{7i} and J_{8i} are set to match the position of J_{7i_obj} and J_{8i_obj}. J_{5i} is directly calculated according to the configuration of the ternary link $J_5J_7J_8$.

$$J_{5i} = \frac{l_{57}}{l_{78}}Rot_z(\varphi_{875})(J_{8i}-J_{7i})+J_{7i} \tag{13}$$

J_{6i} can be derived according to the triangle formed by J_1, J_{5i} and J_{6i}, the derivation is similar to J_{3i} processed in Section 3.1.1).

$$J_{6i} = \frac{l_{56}}{l_{15i}}Rot_z\left(\varphi_{156_i}\right)(J_1-J_{5i})+J_{5i} \tag{14}$$

Hence, J_{3i} and J_{4i} can be acquired according to the configuration of the ternary link $J_3J_4J_7$ the ternary link $J_1J_4J_6$, respectively.

$$J_{4i} = \frac{l_{46}}{l_{16}}Rot_z(\varphi_{164})(J_1-J_{6i})+J_{6i} \tag{15}$$

$$J_{3i} = \frac{l_{37}}{l_{47}}Rot_z(\varphi_{473})(J_{4i}-J_{7i})+J_{7i} \tag{16}$$

The nonlinear constraints are set to make the designed six-bar linkage mechanically practical.

$$\begin{cases} \boldsymbol{f_{1i}}: \dfrac{\left(l_{67i}{}^2+l_{47}{}^2-l_{46}{}^2\right)}{2(l_{67i}*l_{47})} \geq -0.9, i=1,2,\ldots,6 \\ \boldsymbol{f_{2i}}: \dfrac{\left(l_{13i}{}^2+l_{12}{}^2-l_{23}{}^2\right)}{2(l_{13i}*l_{12})} \geq -0.9, i=1,2,\ldots,6 \\ \boldsymbol{f_3}: 0.9 \geq \dfrac{J_{2_6}-J_{3_6}}{l_{23}}\cdot\dfrac{J_{4_6}-J_{3_6}}{l_{34}} \geq -0.9 \\ \boldsymbol{f_4}: 0.9 \geq \dfrac{J_{6_6}-J_{5_6}}{l_{56}}\cdot\dfrac{J_{7_6}-J_{5_6}}{l_{57}} \geq -0.9 \\ \boldsymbol{f_{5i}}: u_{j-1_{deg}} > u_{j_{deg}}, j=2,3,\ldots,6 \\ \boldsymbol{g_1}: l_{56} \geq 20 \\ \boldsymbol{g_2}: l_{57} \geq 5 \\ \boldsymbol{g_3}: l_{23} \geq 10 \end{cases} \tag{17}$$

Table 2 The desired J_{7i_obj} and J_{8i_obj}

	x (mm)	y (mm)
J_{71_obj}	26.3790	−30.2501
J_{81_obj}	51.2323	−15.3064
J_{72_obj}	23.6551	−36.1669
J_{82_obj}	51.4878	−28.0220
J_{73_obj}	20.3848	−42.6389
J_{83_obj}	49.1197	−46.5509
J_{74_obj}	16.2638	−48.9087
J_{84_obj}	37.6439	−68.5019
J_{75_obj}	13.3235	−51.4199
J_{85_obj}	25.7142	−77.6395
J_{76_obj}	9.3118	−52.1835
J_{86_obj}	14.3160	−80.7484

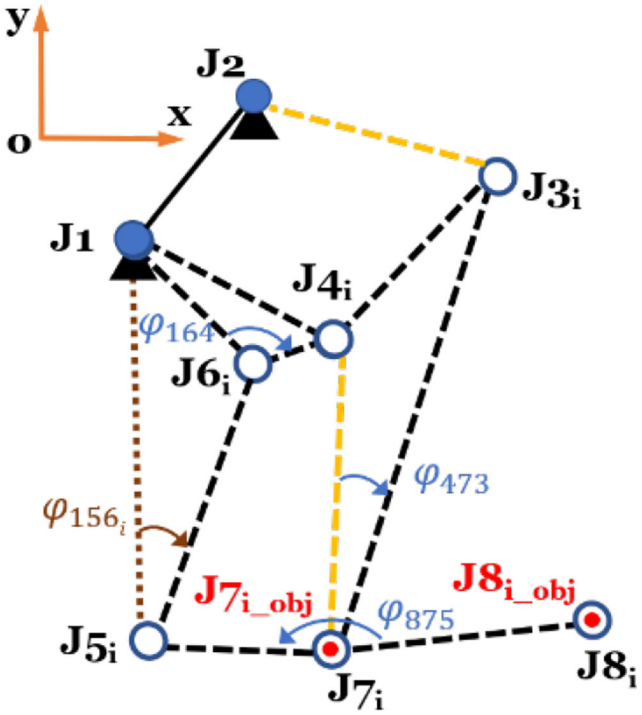

Fig. 7 Demonstration of the parameters in the optimization

where f_{1i} and f_{2i} are designed to guarantee the triangular shapes which are used in the forward kinematic calculation of the optimized six-bar linkage mechanism as mentioned in Section 3.1.1. f_3 and f_4 are set to avoid the dead point where −0.9 and 0.9 are the minimum threshold and the maximum threshold. f_{5i} set to guarantee the monotonicity of u_j. $g_1 - g_3$ are used to make the fabrication of the related links convenient.

The optimal solution is searched using *fmincon* with an interior-point algorithm in MATLAB when the coordinates of $J_1 - J_6$ are limited within [−80, 80] *mm*. The output J_{7i} and J_{8i} are shown in Table 3 with the optimal solution presented in Table 4 with the value of the objective function is 0.254088 when all the constraints are satisfied. ΔJ_{7i}, the difference in the coordinates between J_{7i} and J_{7i_obj} and ΔJ_{8i}, the difference between J_{8i} and J_{8i_obj} are shown in Table 5 as the performance index. The smaller value of the performance index means the better match of the desired points and the output points. Most of the values of the performance are smaller than 1 *mm* while ΔJ_{8_3}, ΔJ_{8_4}, ΔJ_{8_5} and ΔJ_{7_6} are larger than 1 *mm* but smaller than 2.5 *mm*.

Table 3 The output J_{7i} and J_{8i}

	x (*mm*)	*y* (*mm*)
J_{71}	26.5160	−30.1864
J_{81}	51.0489	−14.7223
J_{72}	24.0506	−36.4160
J_{82}	52.0251	−28.7725
J_{73}	20.3670	−42.8932
J_{83}	48.9453	−47.8207
J_{74}	15.6914	−48.3601
J_{84}	38.2139	−66.6286
J_{75}	12.8208	−50.8972
J_{85}	27.4920	−75.9123
J_{76}	10.7771	−52.4403
J_{86}	14.3873	−81.2147

Table 4 The optimal solutions

	value (*mm*)
J_{1_x}	17.5962
J_{1_y}	28.8298
J_{2_x}	27.5962
J_{2_y}	41.9765
J_{3_x}	67.8052
J_{3_y}	79.9999
J_{4_x}	48.6976
J_{4_y}	54.2711
J_{5_x}	22.3051
J_{5_y}	−30.6493
J_{6_x}	38.6975
J_{6_y}	20.1265

$$\begin{cases} \Delta J_{7_i} = \left\| J_{7_i} - J_{7_{iobj}} \right\|_2 \\ \Delta J_{8_i} = \left\| J_{8_i} - J_{8_{iobj}} \right\|_2 \end{cases} \tag{18}$$

The trajectories of the designed six-bar linkage are presented in Fig. 8, where Fig. 8(A) shows the differences between the desired points in red and the output points in blue. The output trajectories in blue match the desired trajectories from *X. laevis's* foot in red well as shown in Fig. 8(B).

3.2 Design of a Spatial Swimming Mechanism to Mimic the Webbed Foot

Apart from the extension of the legs in the power swimming phase, frogs also utilize their webbed foot to minimize the drag force in the recovery phase. The swimming efficiency is improved with the strategy of using the webbed foot. Inspired from this swimming locomotion of frogs, the mechanism to mimic the actuation of the webbed foot is important to improve the swimming performance of the designed mechanism.

Instead of directly assembling an actuator on foot which can be found in [13, 15, 33, 34] which will cause

Table 5 The performance index

	ΔJ_{7_1}	ΔJ_{8_1}	ΔJ_{7_2}	ΔJ_{8_2}	ΔJ_{7_3}	ΔJ_{8_3}	ΔJ_{7_4}	ΔJ_{8_4}	ΔJ_{7_5}	ΔJ_{8_5}	ΔJ_{7_6}	ΔJ_{8_6}
value (*mm*)	0.1511	0.6122	0.4674	0.9230	0.2549	1.2817	0.7928	1.9581	0.7252	2.4787	1.4876	0.4717

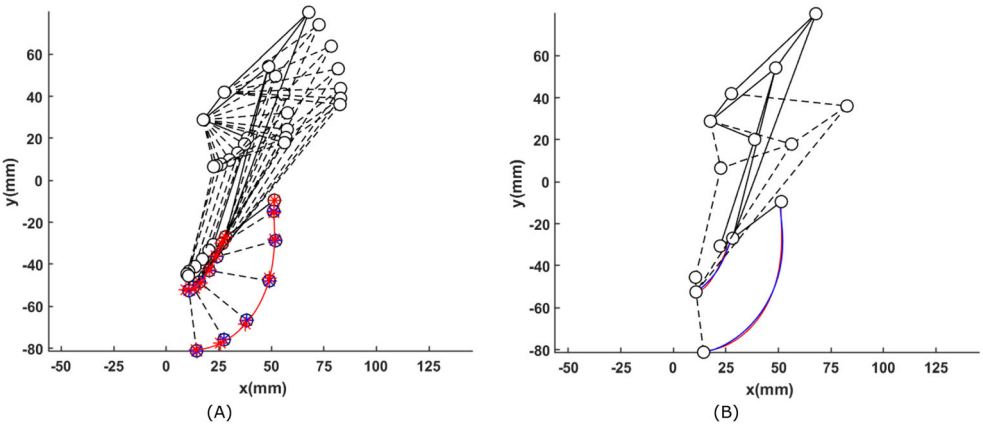

Fig. 8 Optimal design of the six-bar linkage. (**A**) shows the differences between the desired points in red and the output points in blue. The output trajectories in bule match the desired trajectories from *X. laevis's* foot in red well as shown in (**B**)

the problem of waterproofing and add the inertia of the foot, a spatial swimming mechanism is proposed in Fig. 9. The hybrid mechanism is formed by connecting the designed six-bar linkage with a spatial four-bar linkage mechanism. The projected area of the foot is morphed by changing the rotation of the foot, therefore the thrust and drag force is tunable in the swimming locomotion. The schematic of the mechanism is shown in Fig. 9 where Fig. 9(A) shows the 3D model of the hybrid mechanism. The spatial four-bar linkage mechanism is composed of the link HB_1, the linkB_1B_2, the foot which contains joints B_2 $J_{7\_f}J_{8\_f}$ and the planar six-bar linkage. The joints H, $J_{7\_f,}$ and J_{8_f} is the revolute joints while the joint B_2 is a universal joint. B2 is the spherical joint as shown in Fig. 9(B). Actuator 1 drives the six-bar linkage to mimic the leg motion of *X. laevis* while Actuator 2 actuates the joint H to make B_2 rotate about $J_{7\ \_\ f}$ and $J_{8\ \_\ f.}$

Dynamixel XL-320 is selected as the actuator as the motor is fully integrated with position control with PID control by using the control board OpenCM and the motor is compact and light as the size is 24x36x27 *mm* when the weight is only 16.7 *g*. It is convenient to conduct the fast validation of the prototype with the integrated position control. As shown in Fig. 10, the error between the input position and the measured position is acceptable and the delay of the response is negligible when the designed mechanism works in water.

Assuming the direction of the swimming is in the direction of the **y**-axis and the plane $B_2J_{7\ \_\ f}J_{8\ \_\ f}$ is parallel to plane **x-o-**

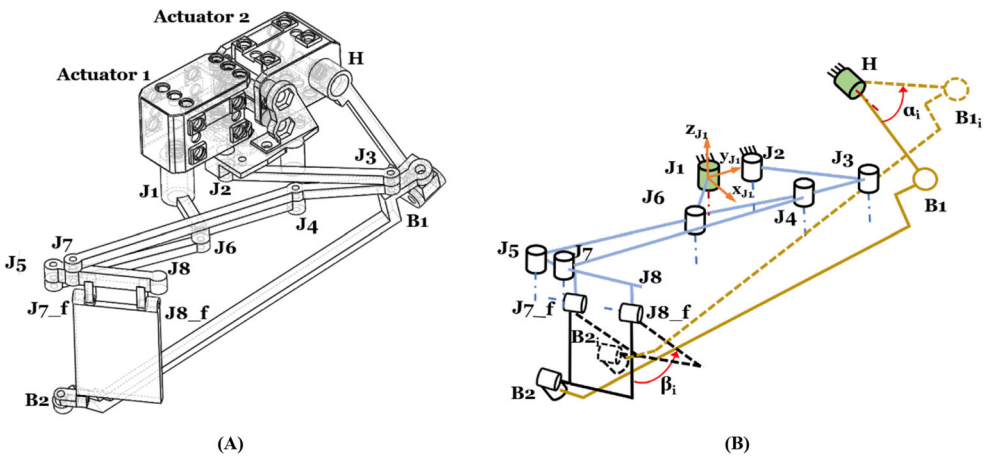

Fig. 9 (**A**) 3D model of the two-DOF hybrid mechanism. (**B**) Schematic of the two-DOF mechanism

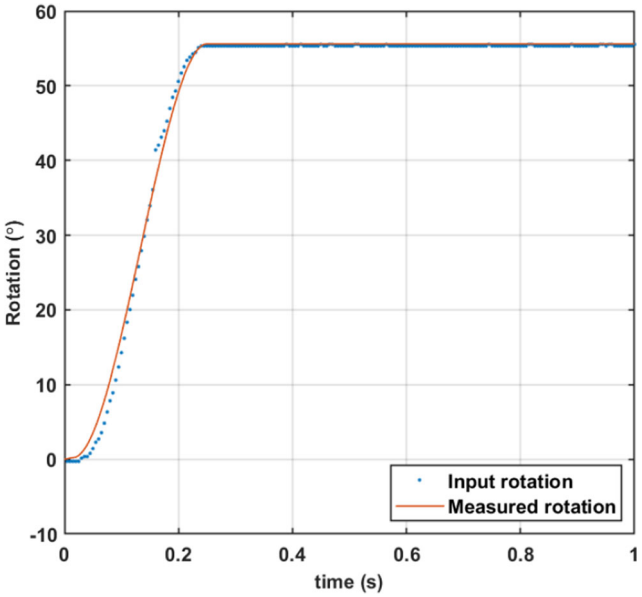

Fig. 10 Rotation measured as the motor driving the foot which submerged in water

z, the area of the foot projected in the **y**-direction is written as

$$S_y = S_0 cos(\beta_i) \tag{19}$$

where S_0 is the area of the foot simplified as an orthogon in this study.

α_i denotes the rotation starting from the **y**-axis can be solved with a given β_i from the equations below

$$\begin{cases} B_{2i} = R_{\boldsymbol{J_{7\_f}J_{8\_f}}}(\beta_i) \\ B_{1i} = Rot_x(\alpha_i)(B_1 - H) + H \\ \|B_{2i} - B_{1i}\| = \|B_2 - B_1\| \end{cases} \tag{20}$$

where $R_{\boldsymbol{J_{7\_f}J_{8\_f}}}(\beta_i)$ is transformation represent the rotation β_i about $J_{7\_f}\vec{J}_{8\_f}$ and B_{2i} in $\{O_{J_1}\}$ can be written as

$$\begin{cases} [B_{2i}]_{O_{J_1}} = d[\boldsymbol{n_x} \quad \boldsymbol{n_y} \quad \boldsymbol{n_z}] \begin{bmatrix} cos(\beta_i) \\ sin(\beta_i) \\ 0 \end{bmatrix} + [J_{7\_f}]_{O_{J_1}} \\ \boldsymbol{n_x} = -\boldsymbol{o}_{J_1}\boldsymbol{z}_{J_1} \\ \boldsymbol{n_z} = \dfrac{\boldsymbol{J_{7\_f}J_{8\_f}}}{l_{78}} \\ \boldsymbol{n_y} = \boldsymbol{n_z} \times \boldsymbol{n_x} \end{cases} \tag{21}$$

In Eq. (21), $d = 42\ mm$ is the distance between B_2 and J_{7_f}. $J_{7\_f}J_{8\_f}$ and J_{8_f} can be calculated from Eqs. (1)–(6) from the six-bar loop. The length of the link HB_1 and B_1B_2 is 56 *mm* and 145 *mm*, respectively.

α_i is solved in one swimming cycle which includes the power swimming phase and the recovery phase. The numerical solutions are presented in Fig. 11(A). In the period $p_1 : t_0(0.5s) - t_1(0.75s)$ the foot rotates backward with the maximized foot area (shown in Fig. 11(B)) with $\beta_i = 0$. The recovery phase starts from $t_1 - t_4$ where in the period $p_2 : t_1(0.75s) - t_2(1.5s)$, u_i keeps constant and β_i increased slowly to 90° to decrease the drag in this period. β_i stays as 90° to decrease the drag in $p_3 : t_2(1.5s) - t_3(2.25s)$ when the leg rotates to the initial state. The foot rotates slowly about $J_{7\_f}\vec{J}_{8\_f}$ in p_4: $t_3(2.25s) - t_4(3.0s)$ when the mechanism recovers to the initial configuration. The configuration of the designed mechanism in one swimming cycle is demonstrated in Fig. 11(B).

4 Hydrodynamic Estimation Based on the Blade Element Model and the Experimental Validation

4.1 Hydrodynamic Estimation Based on Blade Element Model

Researchers proposed the hypothesis that the propulsion generated in frog's swimming is mainly based on drag force and the swimming mechanism is not dominantly the lift-based mechanism [35] The hypothesis is supported by the data from Christoffer's research [14]. Based on the blade element model, the hydrodynamics such as the thrust and drag are estimated and validated in [17]. The basic blade element model for estimating the drag force is written as

$$D = \frac{1}{2}\rho A_p C_d V^2 \tag{22}$$

where, A_p and C_d are the fluid density, the projected area in the direction of movement, and the drag coefficient, respectively. The variation of C_d from 1.1 to 2.0 results in a negligible variation in the net drag generated in the power swimming phase as discussed in [17]. We set C_d = 1.35 with which the estimated model matches the experimental data well. The direction of the drag force D opposes the relative velocity V.

From Eq. (22), the force works as the thrust in the power swimming phase when in the recovery phase, it impedes the propulsion aside from the drag generated from the shape of the frog's body. The velocity of the hindlimbs affects V as the movement of the foot is the cooperation of each joint in the hindlimb. Besides, the webbed foot is used to change A_p to improve the swimming performance. In the proposed design of the spatial mechanism, the velocity of the foot is pertinent to the kinematics of the planar six-bar linkage mechanism with

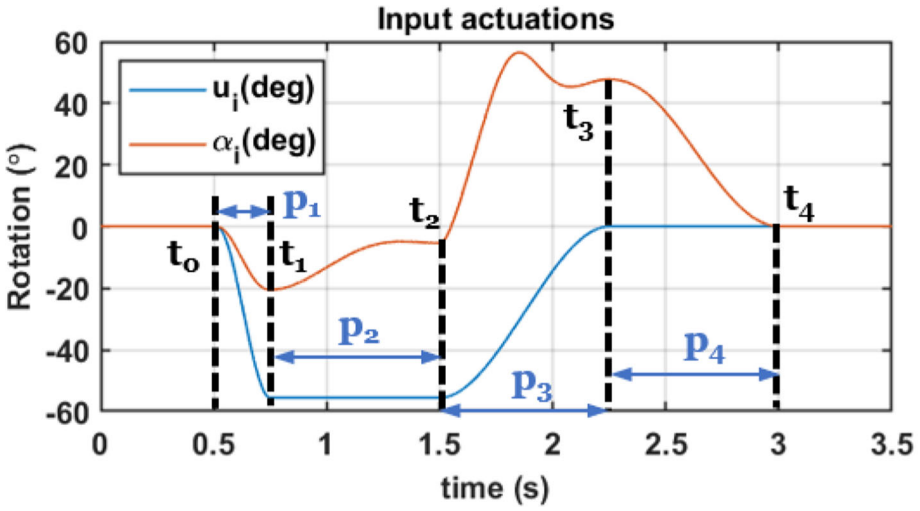

(A)

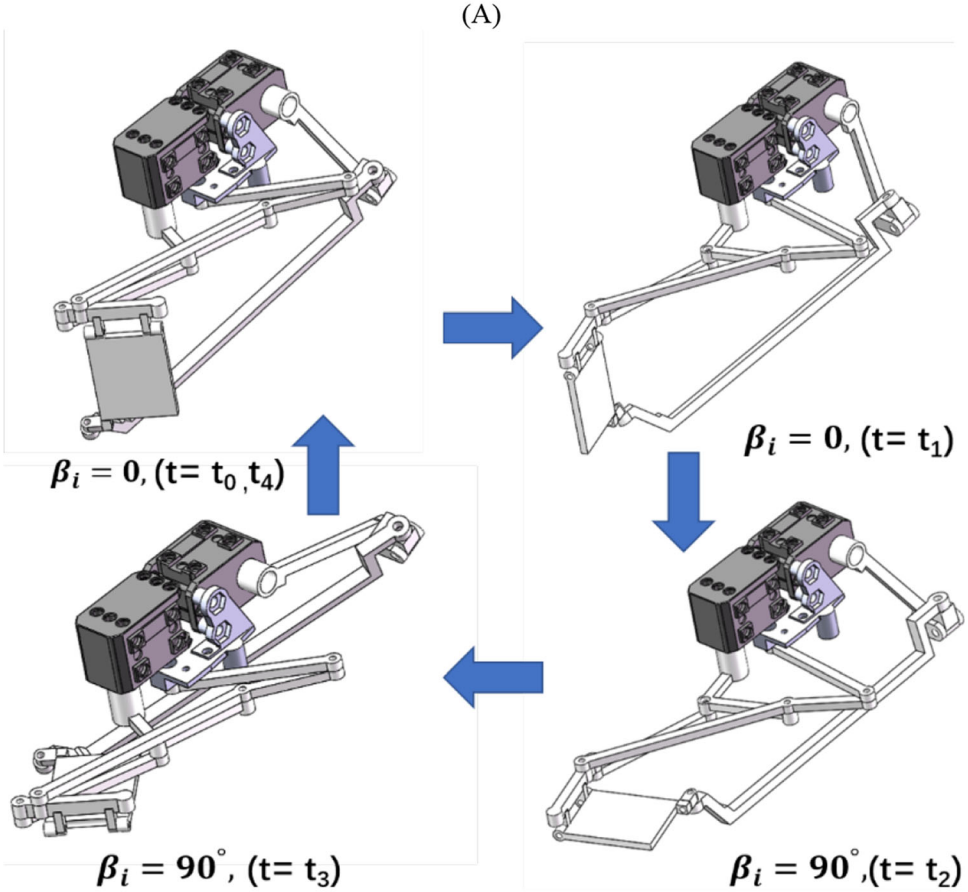

(B)

Fig. 11 The hybrid mechanism mimicking the webbed foot. (**A**) The solutions of α_i with the u_i for one swimming cycle. (**B**). The configuration of the designed mechanism in one swimming cycle

one DoA, and the projected area is controlled by the other DoA from the spatial four-bar linkage.

We focus on the estimation of the thrust in the power swimming phase in which the projected area retains maximum. The body connected to the designed mechanism is fixed. In the recovery phase, the projected area can be controlled theoretically as 0 according to the calculation in Eq. (20), but due to the existence of the width of the link $J_5J_7J_8$, the projected is not 0. Thus, a small force is produced as the drag when the foot rotates back and keeps the projected area minimized. The force in the direction of the movement is demonstrated in Fig. 12 and modeled based on (22) and the mathematical model is expressed as

$$F_y = \int_o^R \rho h C_d cos(\theta_{Foot}) \left(r\omega_{Foot} cos\left(\theta_{foot}\right) + \left(v_{Footy}\right)\right)^2 dr \tag{23}$$

where $v_{Foot} = v_7$ and $R = l_{78}$.

$$\begin{cases}
\left[\dot{J}_{3_\iota}\right]_{O_{J_1}} = -\frac{l_{23}}{{l_{24_i}}^2}\dot{l}_{24_\iota} Rot_z(m_i)\left([J_{4i}]_{O_{J_1}} - [J_2]_{O_{J_1}}\right) + \frac{l_{23}}{l_{24_i}}\dot{Rot}_z(m_\iota)\left([J_{4i}]_{O_{J_1}} - [J_2]_{O_{J_1}}\right) + \frac{l_{23}}{l_{24_i}} Rot_z(m_i)\left[\dot{J}_{4_\iota}\right]_{O_{J_1}} \\
\left[\dot{J}_{4_\iota}\right]_{O_{J_1}} = \dot{Rot}_z(u_\iota)[J_4]_{O_{J_1}} \\
\left[\dot{J}_{5_\iota}\right]_{O_{J_1}} = \frac{l_{56}}{{l_{6_i7_i}}^2}\dot{l}_{6_\iota 7_\iota} Rot_z(n_i)\left([J_{7i}]_{O_{J_1}} - [J_{6i}]_{O_{J_1}}\right) - \frac{l_{56}}{l_{6_i7_i}}\dot{Rot}_z(n_\iota)\left([J_{7i}]_{O_{J_1}} - [J_{6i}]_{O_{J_1}}\right) \\
\qquad - \frac{l_{56}}{l_{6_i7_i}} Rot_z(n_i)\left(\left[\dot{J}_{7_\iota}\right]_{O_{J_1}} - \left[\dot{J}_{6_\iota}\right]_{O_{J_1}}\right) + \left[\dot{J}_{6_\iota}\right]_{O_{J_1}} \\
\left[\dot{J}_{6_\iota}\right]_{O_{J_1}} = \dot{Rot}_z(u_\iota)[J_6]_{O_{J_1}} \\
\left[\dot{J}_{7_\iota}\right]_{O_{J_1}} = \frac{l_{34}}{l_{37}} Rot_z(e)\left(\left[\dot{J}_{4_\iota}\right]_{O_{J_1}} - \left[\dot{J}_{3_\iota}\right]_{O_{J_1}}\right) + \left[\dot{J}_{3_\iota}\right]_{O_{J_1}} \\
\omega_{foot} = \frac{\sqrt{\left(\left[\dot{J}_{7_\iota}\right]_{O_{J_1 x}} - \left[\dot{J}_{5_\iota}\right]_{O_{J_1 x}}\right)^2 + \left(\left[\dot{J}_{7_\iota}\right]_{O_{J_1 y}} - \left[\dot{J}_{5_\iota}\right]_{O_{J_1 y}}\right)^2}}{l_{57}}
\end{cases} \tag{24}$$

ω_{foot} and $\left[\dot{J}_{7i}\right]_{O_{J_1}}$ are presented in Fig. 13(B) and (C) according to Eq. (24).

4.2 The Experimental Validation

The prototype is attached to the force sensor (KunWei KWR75) with the foot submerged in water as shown in Fig. 14. The thrust is generated in the y-direction as shown in Fig. 12 is measured by the force sensor assembled in the sensor mounting bracket. The output motion of the designed prototype is actuated by the motor control board (OpenCM) and powered by the 7.4 V battery. Both the control board and the battery are placed in the 3D printed prototype connector and they are isolated from the water. Two prototypes are assembled when one works for the experiment and the other is used as the backup in case of malfunction. The input actuation is presented in Fig. 11(A) and the communication between the motor control board and the computer is tethered.

Although the size of the water tank is as large as 1.2 × 0.5 × 0.5 m, the generated force by the actuation of the designed prototype makes the water oscillate. The oscillation produced the force on the foot when the water contacts the foot. The force is observed in the experiment as shown in Fig. 15(A) after the period p_1 when the actuation shown in Fig. 11(A) is applied to the prototype. To minimize the effect of the oscillation of water, we measure the generated force separately as the input actuation in p_1, p_2, p_3 and p_4. The reactive force works as the thrust in the period p_1 and p_4 while it works as the drag in the p_2 and p_3. The measurement conducts 5 times in each period. Each experiment starts when the water becomes stable to avoid oscillation. The measurement of the generated force qualitatively matches the estimated thrust

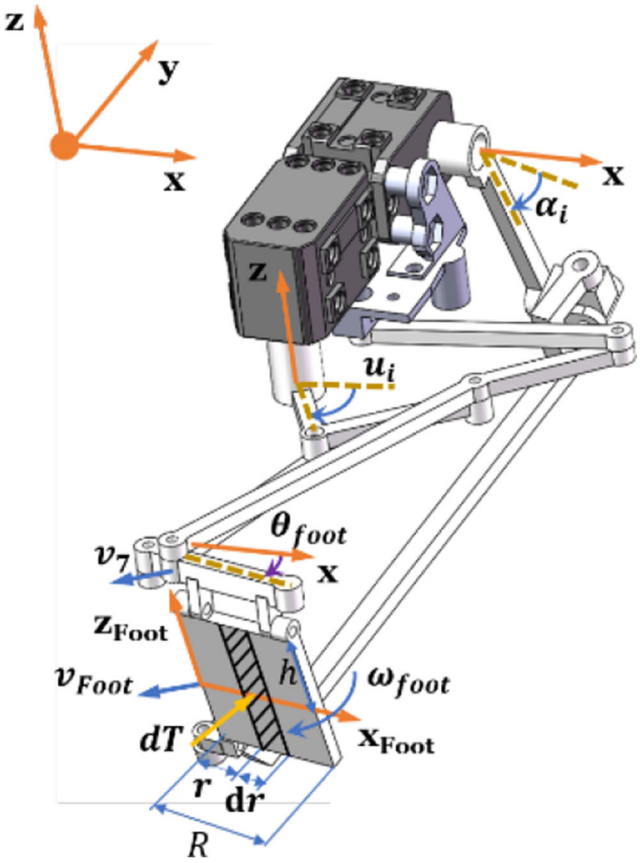

Fig. 12 Demonstration of the thrust generated on the foot

and drag matches calculated from Eq. (23). The peak thrust is around 0.2 N input the actuation corresponding to the period p_1 and the minimum drag is observed as -0.023 N in period p_3. The drag and thrust with respect to the period p_2 and period p_4 are negligible as shown in Fig. 16(A) and (B), respectively. Although the hydrodynamic analysis based on the blade element theory is qualitative as the difference between the simulation result and the experimental data, it is convenient for the fast validation of the mechanism design.

5 Conclusions and Future Work

In this paper, a novel design of a hybrid mechanism that realizes a miniaturization number of DoAs for swimming robots is the major contribution. The design of the mechanism is inspired by the aquatic frog *X. laevis*. To mimic the spatial movement of the footpad of the frog, the hybrid mechanism is composed of a six-bar linkage and a spatial four-bar linkage. The performance of the prototype is estimated based on the blade element theory. The reactive force measured in the experiment validates the efficient performance of the prototype by mimicking the locomotion of *X. laevis* in the power swimming phase and the recovery phase.

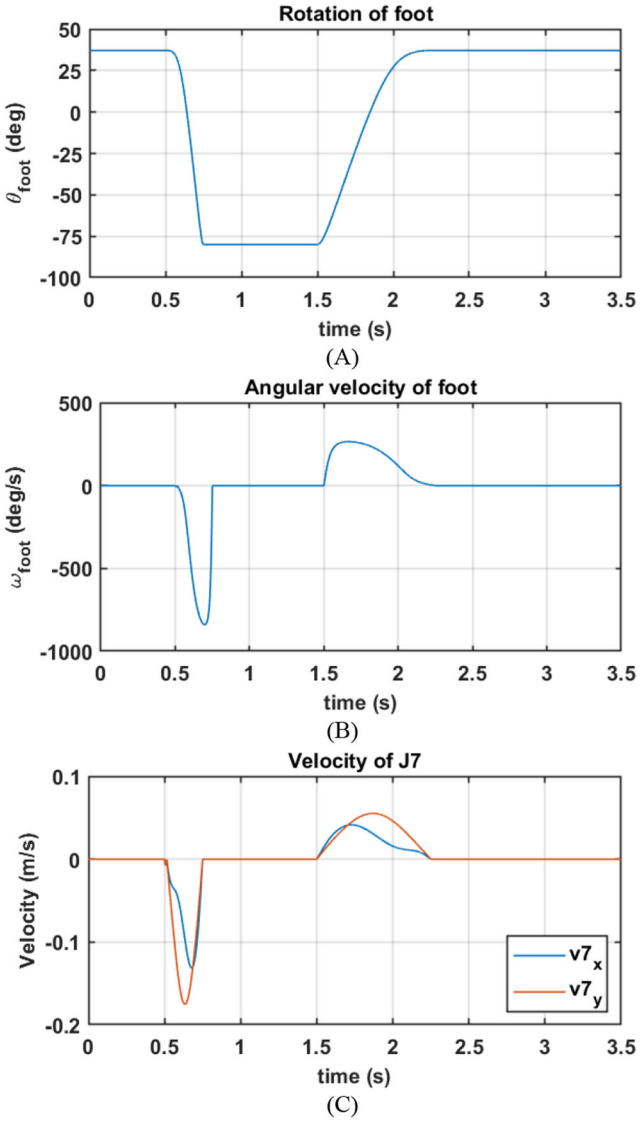

Fig. 13 The kinematic solutions of the foot θ_{foot}, ω_{foot} and v_7 with input actuation of one swimming cycle. (**A**). θ_{foot} with input actuation of one swimming cycle. (**B**). ω_{foot} with input actuation of one swimming cycle. (**C**). v_7 with input actuation of one swimming cycle

A novel optimization of the six-bar linkage for mimicking the locomotion *X. laevis*.'s foot in the frontal plane is proposed. Six pairs of the points from the two desired trajectories are selected according to the analysis of the polynomial system. The two trajectories are tracked well as most of the values in the performance are less than 1 *mm* with one DoA input. The implementation of the spatial four-bar linkage used to mimic the webbed foot simplifies the mechanism with the other DoA input.

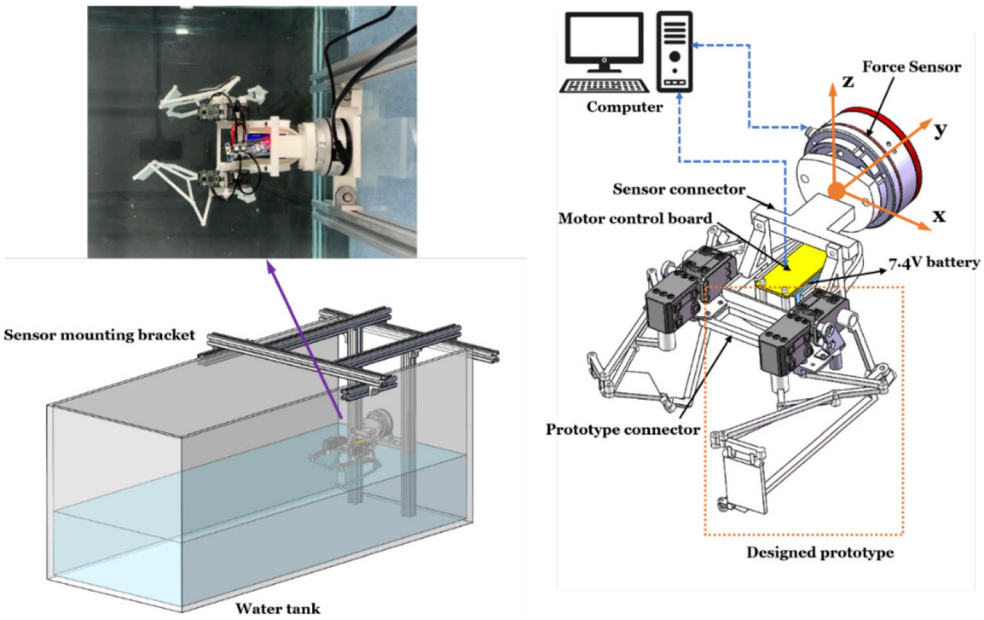

Fig. 14 Experiment setup

The hybrid mechanism is analyzed to mimic the locomotion of both the legs and webbed foot of *X. laevis*. The inversed kinematic analysis is conducted to find the two input actuations when the output motion is desired to mimic the locomotion of *X. laevis*.

Hydrodynamic analysis of the designed spatial mechanism is conducted based on blade element theory despite its inaccuracy. The generated thrust is similar to which generated in the power swimming phase of aquatic frogs. As measured from the experiment, the peak force in the power swimming phase is approximately 0.2 *N* which is dramatically larger than the drag generated in the recovery phase around 0.023 *N*. The huge difference between the reactive force generated in the two phases makes the swimming efficient which attributes to the swimming locomotion inspired from *X. laevis*.

In the future, actuation patterns will be optimized for generating suitable gaits to enhance the highly efficient motion of the robot by applying the motor control method with higher precession. The untethered robot will be designed and fabricated after solving the waterproof

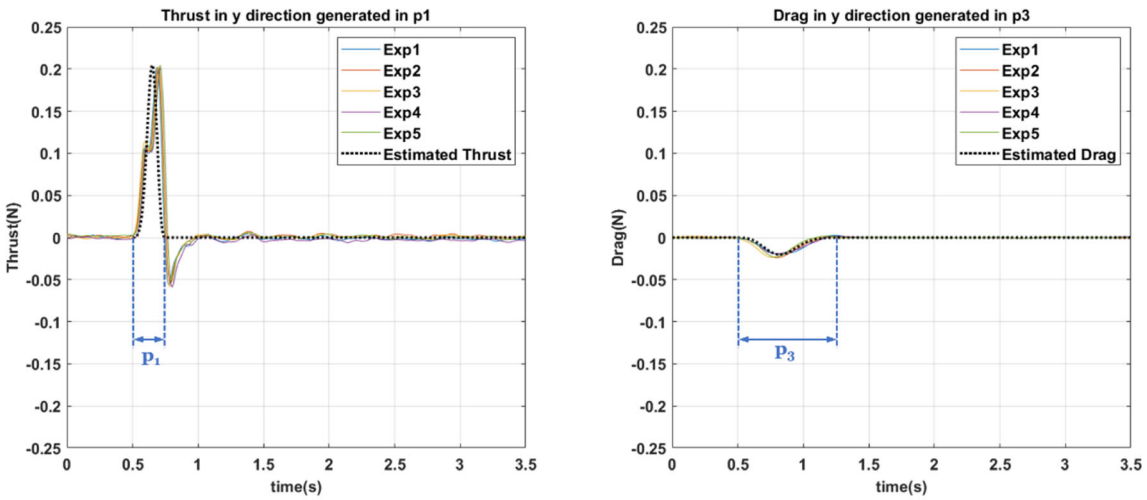

(A) (B)

Fig. 15 The measured force in p_1 and p_3 as well as the estimated force are presented in dotted curve in black. (**A**). The measured and estimated thrust in period p_1. (**B**). The measured and estimated thrust in period p_3

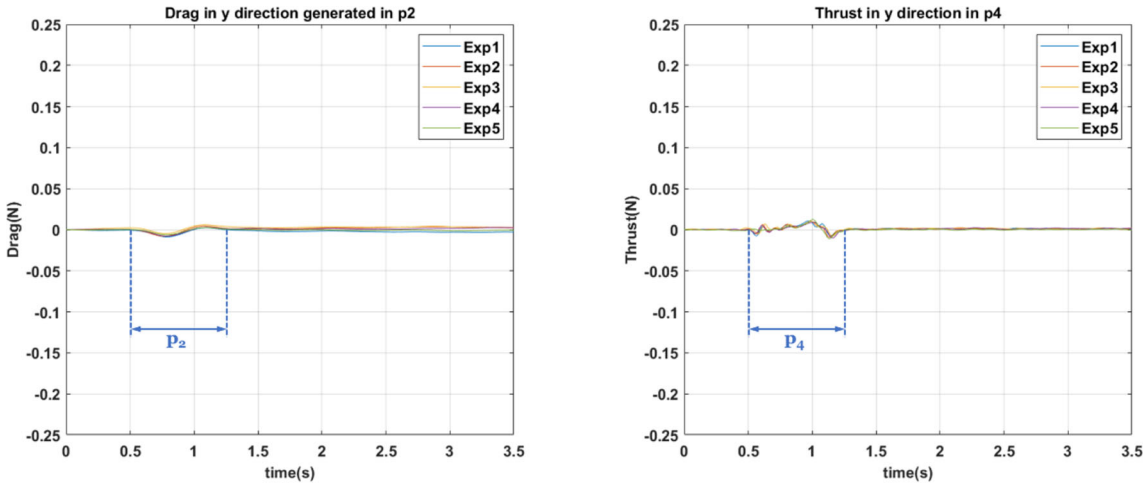

Fig. 16 The measured force in p_1 and p_3. (**A**). The measured drag in period p_2. (**B**). The measured thrust in period p_4

problem. The different swimming gaits including synchronous and asynchronous swimming are needed to generate with the design to explore their swimming efficiency of them. The more precise hydrodynamic analysis will be conducted by using CFD tools to explain the difference between the result from the current estimated model and the experimental data.

Authors Contributions Yucheng Tang conceived the presented idea of the mechanism and organized the whole paper. Xiaolong Yang built the inversed kinematic modeling. Wei Liu built the CAD model and analyzed the assembly simulation. Lizhi Qi proposed multi-objective optimization and selected the design parameters. Yan Wang calculated the kinematic simulation of the designed mechanism. Yulin Wang analyzed the functions of the mechanism and he was responsible for planning and coordinating the steps of the research.

Funding This work was supported by the National Key R&D Program of China (2018YFB2001303), the National Natural Science Foundation of China (Grant No. 52075267), the Natural Science Foundation of Jiangsu Province (Grant no. BK20210341), Grant the Fundamental Research Funds for the Central Universities (Grant No. 309201A8801), and the Open Fund of State Key Laboratory of Intelligent Manufacturing System Technology.

Data Availability Not Applicable.

Declarations This paper does not report research that requires ethical approval. Consent to participate or consent to publish statements is accordingly also not required.

Competing Interests The authors declare that they have no known competing financial interests or personal relationships that could have appeared to influence the work reported in this paper.

References

1. Park, H.S., Floyd, S., Sitti, M.: Roll and pitch motion analysis of a biologically inspired quadruped water runner robot. Int. J. Robot. Res. **29**(10), 1281–1297 (2010). https://doi.org/10.1177/0278364909354391
2. Ramezani, A., Chung, S., Hutchinson, S.: A biomimetic robotic platform to study flight specializations of bats. Sci. Robot. **2**(3), Art-No (2017)
3. Kim, S., Spenko, M., Trujillo, S., Heyneman, B., Santos, D., Cutkoskly, M.R.: Smooth vertical surface climbing with directional adhesion. IEEE Trans. Robot. **24**(1), 65–74 (2008). https://doi.org/10.1109/TRO.2007.909786
4. Zhong, Y., Li, Z., Du, R.: A novel robot fish with wire-driven active body and compliant tail. IEEE/ASME Trans. Mechatronics. **22**(4), 1633–1643 (2017). https://doi.org/10.1109/TMECH.2017.2712820
5. Colorado, J., Barrientos, A., Rossi, C., Breuer, K.: Biomechanics of smart wings in a bat robot morphing wings using SMA actuators. Bioinspir. Biomim. **7**(3), 036006 (2012). https://doi.org/10.1088/1748-3182/8/1/019501
6. Jansson, N., Bale, R., Onishi, K., Tsubokura, M.: Optimizing the structure and movement of a robotic bat with biological kinematic synergies. Int. J. Robot. Res. **37**(10), 1233–1252 (2018). https://doi.org/10.1177/ToBeAssigned
7. Floyd, S., Keegan, T., Palmisano, J., Sitti, M.: A novel water running robot inspired by basilisk lizards. IEEE Int. Conf. Intell. Robot. Syst. **1**, 5430–5436 (2006). https://doi.org/10.1109/IROS.2006.282111
8. Kim, H., Lee, D., Jeong, K., Seo, T.: Water and ground-running robotic platform by repeated motion of six spherical footpads. IEEE/ASME Trans. Mechatronics. **21**(1), 175–183 (2016). https://doi.org/10.1109/TMECH.2015.2435017
9. Park, H.S., Sitti, M.: Compliant footpad design analysis for a bio-inspired quadruped amphibious robot. 2009 IEEE/RSJ Int. Conf. Intell. Robot. Syst. IROS. **2009**, 645–651 (2009). https://doi.org/10.1109/IROS.2009.5354680

10. Crespi, A., Karakasiliotis, K., Guignard, A., Ijspeert, A.J.: Salamandra Robotica II: an amphibious robot to study salamander-like swimming and walking gaits. IEEE Trans. Robot. **29**(2), 308–320 (2013). https://doi.org/10.1109/TRO.2012.2234311
11. Karakasiliotis, K., Thandiackal, R., Melo, K., Horvat, T., Mahabadi, N.K., Tsitkov, S., Cabelguen, J.M., Ijspeert, A.J.: From cineradiography to biorobots: An approach for designing robots to emulate and study animal locomotion. J. R. Soc. Interface. **13**, 119 (2016). https://doi.org/10.1098/rsif.2015.1089
12. Aerts, P., Nauwelaerts, S.: Environmentally induced mechanical feedback in locomotion: frog performance as a model. J. Theor. Biol. **261**(3), 372–378 (2009). https://doi.org/10.1016/j.jtbi.2009.07.042
13. Pandey, J., Reddy, N.S., Ray, R., Shome, S.N.: Biological swimming mechanism analysis and design of robotic frog. 2013 IEEE Int. Conf. Mechatronics Autom. IEEE ICMA. **2013**, 1726–1731 (2013). https://doi.org/10.1109/ICMA.2013.6618176
14. Johansson, L.C., Lauder, G.V.: Hydrodynamics of surface swimming in leopard frogs (*Rana pipiens*). J. Exp. Biol. **207**, 3945–3958 (2004). https://doi.org/10.1242/jeb.01258
15. Fan, J.Z., Zhang, W., Kong, P.C., Cai, H.G., Liu, G.F.: Design and dynamic model of a frog-inspired swimming robot powered by pneumatic muscles. Chinese J. Mech. Eng. English Ed. **30**(5), 1123–1132 (2017). https://doi.org/10.1007/s10033-017-0182-5
16. Fan, J., Wang, S., Yu, Q., Zhu, Y.: Swimming performance of the frog-inspired soft robot. Soft Robot. **7**(5), 615–626 (2020). https://doi.org/10.1089/soro.2019.0094
17. Richards, C.T.: The kinematic determinants of anuran swimming performance: an inverse and forward dynamics approach. J. Exp. Biol. **211**(Pt 19), 3181–3194 (2008). https://doi.org/10.1242/jeb.019844
18. Y. Tang, L. Qin, X. Li, C. Chew, and J. Zhu: A frog-inspired swimming robot based on dielectric elastomer actuators. In 2017 IEEE/RSJ International Conference on Intelligent Robots and Systems (IROS), 2017, pp. 1–6
19. O'Brien, B., Calius, E., Xie, S., Anderson, I.: An experimentally validated model of a dielectric elastomer bending actuator. Proc. SPIE 6927. **6927**, 69270T–69270T–11 (2008). https://doi.org/10.1117/12.776098
20. O'Brien, B., McKay, T., Calius, E., Xie, S., Anderson, I.: Finite element modelling of dielectric elastomer minimum energy structures. Appl. Phys. A Mater. Sci. Process. **94**(3), 507–514 (2009). https://doi.org/10.1007/s00339-008-4946-8
21. Zhao, J., et al.: Equivalent dynamic model of DEMES rotary joint. Smart Mater. Struct. **25**(7), 75025 (2016)
22. Kargo, W.J., Nelson, F., Rome, L.C.: Jumping in frogs: assessing the design of the skeletal system by anatomically realistic modeling and forward dynamic simulation. J Exp Biol. **205**(12), 1683–1702 (2002) [Online]. Available: http://www.ncbi.nlm.nih.gov/pubmed/12042328
23. A. J. Collings, L. B. Porro, C. Hill, and C. T. Richards: The impact of pelvic lateral rotation on hindlimb kinematics and stride length in the red-legged running frog, *Kassina maculata*. R. Soc. Open Sci., vol. 6, no. 5, 2019. https://doi.org/10.1098/rsos.190060
24. Kargo, W.J., Rome, L.C.: Functional morphology of proximal hindlimb muscles in the frog Rana pipiens. J. Exp. Biol. **205**(2002), 1987–2004 (2002)
25. Haldane, D.W., Plecnik, M.M., Yim, J.K., Fearing, R.S.: Robotic vertical jumping agility via series-elastic power modulation. Sci. Robot. **1**(1), eaag2048 (2016). https://doi.org/10.1126/scirobotics.aag2048
26. Richards, C.T.: Kinematics and hydrodynamics analysis of swimming anurans reveals striking inter-specific differences in the mechanism for producing thrust. J. Exp. Biol. **213**(4), 621–634 (2010). https://doi.org/10.1242/jeb.032631
27. Richards, C.T., Clemente, C.J.: Built for rowing: frog muscle is tuned to limb morphology to power swimming. J. R. Soc. Interface. **10**, 20130236 (2013). https://doi.org/10.1098/rsif.2013.0236
28. Plecnik, M.M., Michael McCarthy, J.: Numerical Synthesis of Six-Bar Linkages for Mechanical Computation. J. Mech. Robot. **6**(3), 031012 (2014). https://doi.org/10.1115/1.4027443
29. Plecnik, M.M., McCarthy, J.M.: Kinematic synthesis of Stephenson III six-bar function generators. Mech. Mach. Theory. **97**, 112–126 (2016). https://doi.org/10.1016/j.mechmachtheory.2015.10.004
30. Plecnik, M.M., McCarthy, J.M.: Design of Stephenson linkages that guide a point along a specified trajectory. Mech. Mach. Theory. **96**, 38–51 (2016). https://doi.org/10.1016/j.mechmachtheory.2015.08.015
31. Plecnik, M.M., McCarthy, J.M.: Computational Design of Stephenson II six-Bar function generators for 11 accuracy points. J. Mech. Robot. **8**(1), 1–9 (2016). https://doi.org/10.1115/1.4031124
32. Huang, H., Brown, D.D.: Overexpression of Xenopus laevis growth hormone stimulates growth of tadpoles and frogs. Proc. Natl. Acad. Sci. U. S. A. **97**(1), 190–194 (2000). https://doi.org/10.1073/pnas.97.1.190
33. Kashem, S.B.A., Jawed, S., Ahmed, J., Qidwai, U.: Design and implementation of a quadruped amphibious robot using duck feet. Robotics. **8**(3), 77 (2019). https://doi.org/10.3390/robotics8030077
34. S. Guo et al.: Basic characteristics evaluation of a duck-like robot. Proc. 2019 IEEE Int. Conf. Mechatronics Autom. ICMA 2019, pp. 1502–1507, 2019. https://doi.org/10.1109/ICMA.2019.8816536
35. Gal, J.M., Blake, R.W.: Biomechanics of frog swimming I. estimation of the force generated by Hymenochirus boettgeri. J. Exp. Biol. **138**, 399–411 (1988)

Yucheng Tang received the B.S. degree in mechanical engineering from Nanjing University of Science and Technology, Nanjing, China, in 2013. He is currently a Ph.D. candidate in mechanical engineering with Nanjing University of Science and Technology. His current research interests include mechanisms and robotics, bio-inspired robotics and mechanism design.

Xiaolong Yang received the B.S. degree in mechanical engineering and automation in 2011 and the M.S. and Ph.D. degrees in mechatronic engineering in 2014 and 2018, all from Nanjing University of Aeronautics and Astronautics. From 2018 to 2019, he was a Postdoctoral Fellow and Mechatronics Laboratory Director with the Lab of Biomechatronics and Intelligent Robotics in the Mechanical Engineering Department at City University of New York, City College, US. Currently, he is an associate professor with School of Mechanical Engineering, Nanjing University of Science and Technology. His research interests include robotics, exoskeletons, parallel mechanism.

Wei Liu received the B.S. degree and the Ph.D. degree in mechanical engineering from China Aerospace Science and Technology Corporation in 1998 and 2011, respectively. Currently, he is the academic leader of the State Key Laboratory of Intelligent Manufacturing System Technology. From 1998, his research interests include structure design, strength analysis, environment test, motion simulation, assembly process of compliance products and intelligent manufacturing.

Lizhi Qi is a professor in robotics at Paris-Saclay University, France. He received his M.Sc. and Ph.D. in physics from University of Technology of Compiègne, France in 1994 and 1998 respectively. His research interests include robotics, autonomous vehicles, sensors, and communication.

Yan Wang is a professor in robotics at Paris-Saclay University, France. He received his M.Sc. and Ph.D. in physics from University of Technology of Compiègne, France in 1994 and 1998 respectively. His research interests include robotics, autonomous vehicles, sensors, and communication.

Yulin Wang received the B.S. degree from Nanjing University of Aeronautics and Astronautics, Nanjing, China, in 2003 and the Ph.D. degree from Shanghai Jiao Tong University, Shanghai, China, in 2009. Currently, he is a full professor with the School of Mechanical Engineering, Nanjing University of Science and Technology. His current research interests include intelligent robot, advanced manufacturing technology and precision measurement and control technology.